Near Ultraviolet Photoresponse of a Silicon Carbide and Tantalum Boride Heterostructure

Haroldo T. Hattori, *Senior Member, IEEE*, Sanjida Akter, Ibrahim A. M. Al-Ani, and Ziyuan Li, *Senior Member, IEEE*

***Abstract*—Silicon carbide (SiC) is widely used in abrasives, heating devices, light emitting diodes and high-power electronics, because of its unique physical-chemical properties including high hardness, high melting point, excellent thermal conductivity, and wide bandgap. In recent years, its color centers have also been used as potential sources of single photons. Given that borides and carbides are refractory materials, we decided to study a heterostructure formed by an n-doped silicon carbide substrate and a layer of tantalum monoboride (TaB) for near ultraviolet (UV) photodetection. It is shown that the addition of TaB creates a rectifying device that can handle currents higher than 300 mA, showing its potential for high-power optoelectronic devices. The detector also has a high responsivity of 2.9 A/W at the free-space wavelength of 405 nm and a fast frequency response of 610 kHz. The high performance of the detector is attributed to the high thermal and electrical conductivity, large bandgap of SiC, and its moderately close match in atomic arrangement with TaB. Such heterostructure offers a simple method to produce high-performance near UV photodetectors operating under hard conditions such as high power, high temperature and corrosive or oxidizing environments.**

***Index Terms*—Silicon carbide, ultraviolet response, tantalum boride, photodetector.**

I. Introduction

Silicon carbide (SiC) is a wide bandgap semiconductor that has been used in many different areas such as power electronics (it can withstand high voltages), automotive industry and quantum sensing [1]. It has different crystalline structures, with the most common structures being 3C (zinc blend cubic structure), 4H and 6H (both having a hexagonal structure). In case of 6H-SiC, its bandgap is 3.02 eV, and its lattice constants are 3.08 Å (in-plane) and 15.12 Å (out-of-plane c-axis) [2]. The mobility of doped SiC depends on the doping concentration: for example, with an n-doping concentration of 10^{18} cm^{-3}, the electron mobility is around 300 $cm^2/(Vs)$, while the low doping concentration can reach values above 1140 $cm^2/(Vs)$ [3]. Also, the mobility has a variation with temperature proportional to $(T/300)^{-2.70}$ where T is the temperature in Kelvin. Due to its large bandgap, silicon carbide devices can operate at temperatures above 1000 °C.

Silicon carbide can absorb light at wavelengths below 400 nm, being suitable for constructing ultraviolet (UV) photodetectors. In general, many UV photodetectors have found applications in areas such as environmental sensing, polarization imaging [4], artificial intelligence and autonomous vehicles [5]. They are generally based on wide bandgap semiconductors such as silicon carbide [6], [7], gallium oxide [8], [9], [10], gallium nitride [11], [12], zinc oxide [13], [14], [15], [16], other oxides [17] and polymers [18]. In our case, a photodetector is constructed on top of an n-doped silicon carbide substrate with a carrier concentration of 10^{18} cm^{-3} by adding a thin layer of tantalum monoboride (TaB) on top of the substrate.

On the other hand, metal borides are well known for their high temperature melting points, high mechanical strength and resistance to oxidation and corrosion [19], [20], being widely used in protective armour, nuclear reactors, and mechanical cutting tools [20]. In addition, boron is widely added to metals to reduce wear and corrosion. Metal borides have also been sintered with silicon carbide to improve hardness and mechanical resistance [20].

There are many different allotropes of tantalum and boride such as TaB, Ta_5B_6, Ta_3B_4 and TaB_2, - these borides have high melting point, are extremely hard and have high electrical and thermal conductivity [21]. TaB has an orthorhombic crystalline structure (Cmcm space group) with lattice constants of 4.66, 4.66 and 3.172 angstroms and angles of 90, 90 and 138.596 degrees, respectively. It is a non-magnetic material with a Vickers hardness between 2330 and 2530 kgf mm^{-2} [20], melting point above 3000 °C and is resistant to acids and oxidation [22]. All these properties make TaB an attractive material for devices working in harsh environments (e.g., with high temperatures and mechanical stress).

Given the interesting properties of both materials, we decided to construct a heterostructure by combing silicon carbide and tantalum monoboride and study its main opto-electronic properties. We show that the addition of TaB to a nitrogen n-doped 6H silicon carbide substrate leads to the formation of a diode junction with high responsivity at 405 nm (maximum of 3.0 A/W at low powers and 0.2 A/W at higher powers) and capability of working at electrical frequencies as high as 610 kHz.

Manuscript received 10 January 2023; revised 10 February 2023; accepted 14 February 2023. Date of publication 17 February 2023; date of current version 15 March 2023. This work was supported by the Australian National Fabrication Facility, ACT node. *(Corresponding author: Ziyuan Li.)*

Haroldo T. Hattori, Sanjida Akter, and Ibrahim A. M. Al-Ani are with the School of Engineering and Information Technology, UNSW Canberra, Canberra ACT 2610, Australia (e-mail: h.hattori@adfa.edu.au; sanjida.akter@adfa.edu.au; i.al-ani@student.adfa.edu.au).

Ziyuan Li is with the MoE Key Lab of Photoelectronic Imaging Technology and System, School of Optics and Photonics, Beijing Institute of Technology, Beijing 100081, China (e-mail: ziyuan.li@bit.edu.cn).

This article has supplementary downloadable material available at https://doi.org/10.1109/JPHOT.2023.3246167, provided by the authors.

Digital Object Identifier 10.1109/JPHOT.2023.3246167

This work is licensed under a Creative Commons Attribution 4.0 License. For more information, see https://creativecommons.org/licenses/by/4.0/

II. Experimental Section

Experiments start with a commercial 10 mm by 10 mm 6H n-type silicon carbide substrate, purchased from MSE supplies. The sample has a thickness of 350 μm, with doping concentration of 10^{18} cm^{-3}, electrical resistivity between 0.015 and 0.025 Ω-cm. The datasheet states that the refractive indices at the free-space wavelength of 750 nm are 2.61 and 2.66, consistent with data from Wang et al. [23]. Its bandgap energy is 3.23 eV, meaning that the sample absorbs light mostly at free-space wavelengths below 380 nm.

A. Deposition of TaB Layer

The initial step was to deposit TaB using DC sputtering (AJA ATC-2200 system) for 30 minutes on a silicon substrate to measure its deposition rate. The sputtering DC power was 400 W, with argon acting as a sputtering gas with a flow rate of 20 sccm, under a chamber pressure of 4 mTorr. The thickness of the deposited material was then measured with a Dektak surface profiler: based upon the measurement of the thickness and the 30 minutes deposition time, the deposition rate is about 2.45 nm/min. After that, the commercial SiC substrate was cleaned with isopropyl alcohol and acetone in an ultrasonic cleaner. 1% hydrofluoric acid (HF) was then used to remove the native oxide on the substrate surface, followed by the deposition of a TaB layer on the substrate by using the sputtering system for 220 minutes, leading to a thickness of 540 nm. The refractive indices of the TaB layer were then measured by a JA Woollam M-2000D ellipsometer.

B. Device Fabrication

After depositing the TaB layer, top and bottom electrodes are added to the device by depositing 190 nm aluminium layers on the top and bottom of the sample via an electron beam thermal evaporator, as shown in Fig. 1(a). The bottom contact covers the whole area of the substrate.

C. Optical Characterization and Measurement

The devices were characterized by using a S1FC405 Thorlabs laser. The laser emits light at the free-space wavelength of 405 nm, which is coupled to a single mode fiber. The maximum measured power at the output is 10 mW. Light leaving the fiber is collimated by a TC06FC-405 fiber collimator, which leads to a beam spot-diameter of 1.10 mm at the output of the collimator. Also, a Q-switched laser was used to analyze the time response of the devices with pulse duration of 10 ns. The photocurrent as a function of applied voltage was measured with a Keithley 2450 source meter with resolution of 10 nA.

D. Electrical Characterization of the TaB Film

A four-point probe T2001A3 from Ossila was used to electrically characterize the TaB sputtered film. TaB is a refractory metallic ceramic (no bandgap) with high conductivity. The measured conductivity was around 160 kS/m, while the calculated electron concentration is about $n = 3 \times 10^{23}$ cm^{-3}.

(a)

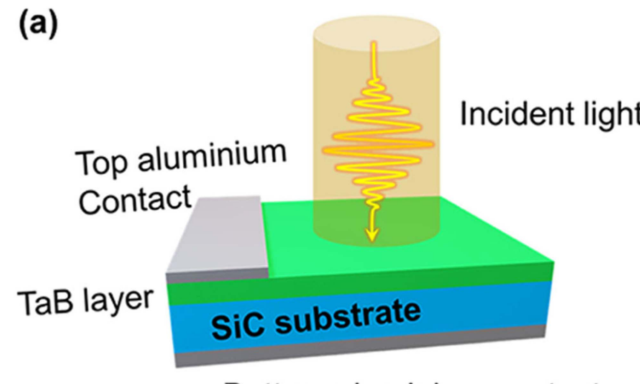

(b)

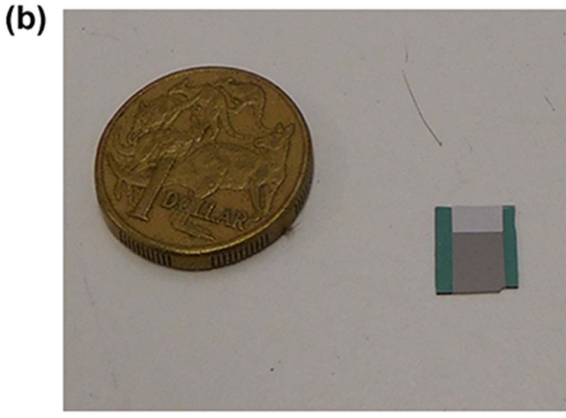

Fig. 1. (a) Schematic view of the photodetector. (b) Top photograph of the detector compared with a one Australian dollar coin.

If the conductivity (σ) is given by $\sigma = en\mu_e$ (e is the electron charge), then its electron mobility is calculated as $\mu_e = 3.39 \times 10^{-2}\ \mathrm{cm}^2/(\mathrm{V}\cdot\mathrm{s})$.

III. Results and Discussion

A top view photograph of the fabricated device is shown in Fig. 1(b) and compared with a one Australian dollar coin. The area of the substrate is around 10 mm by 10 mm: after subtracting the area occupied by the metallic (reflective) contacts, the useful area of the detector is around 7 mm by 6 mm. In the photograph, the green areas show the non-sputtered areas where the sample holder held the device in the sputtering system.

Fig. 2(a) shows a scanning electron microscopy (SEM) image of the cross section of the device (an extra layer of platinum was deposited on top of the TaB layer to reduce charging of the SEM probe). The thickness of the TaB layer is 540 nm as shown in the Figure and it seems to have been smoothly deposited on the silicon carbide substrate. The TaB thickness is chosen so that most of the incident light at 405 nm is absorbed by the material while minimizing the reflectance of the device. The interface between SiC and TaB seems to be reasonably smooth, similarly to other borides deposited by sputter (e.g.,

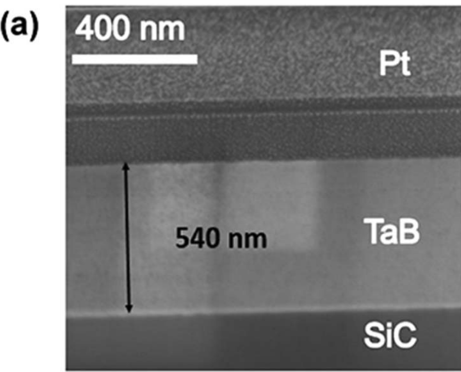

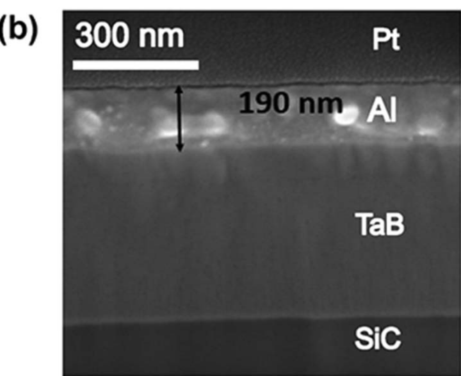

Fig. 2. SEM image of the cross section of the device after (a) TaB and (b) Al deposition.

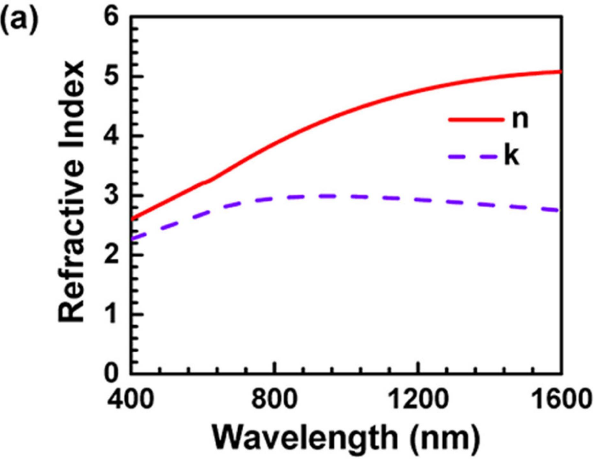

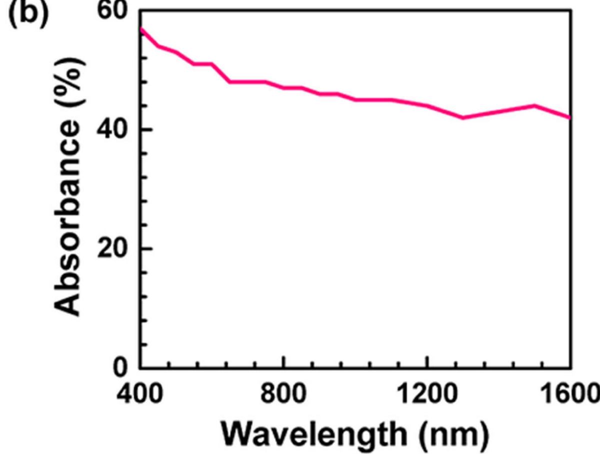

Fig. 3. (a) Measured refractive index (real and imaginary parts are represented by solid and dotted curves, respectively) of tantalum monoboride. (b) Theoretical absorbance as a function of the wavelength.

tungsten monoboride) [24]. Fig. 2(b) shows the region with the top aluminium electrode (thickness of around 190 nm): although aluminium was deposited by an electron beam evaporator, the metallic region seems to be a bit granular. The interface between the TaB layer and the top aluminium contact seems to be smooth.

Fig. 3(a) shows the real (n, red solid curve) and imaginary (k, violet dotted curve) parts of the measured refractive index of tantalum monoboride as a function of the wavelength. The refractive index at 400 nm is about 2.6-j2.27. Moreover, the imaginary part of the refractive index remains high even for wavelengths beyond 1600 nm, indicating that TaB has the enormous potential for ultrawide photodetection covering both visible and infrared ranges. On the other hand, 6H silicon carbide has large bandgap and thus cannot absorb light at wavelengths above 380 nm. The integration of TaB on such a large band gap material to develop photodiodes with p−n heterojunctions may drastically reduce minority carriers on either side of the junction, leading to a much reduced reverse biased dark current [25].

Based on the measured refractive indices, the absorbance as a function of the wavelength was calculated by using the finite difference time-domain (FDTD) method. The refractive indices for silicon carbide were taken from reference [23], while the measured refractive indices were also used in the calculations. The maximum absorbance occurs for a thickness of 200 nm for TaB. At the free-space wavelength of 405 nm, the absorbance of the device is about 60%. The absorbance is above 50% for wavelengths up to 700 nm as shown in Fig. 3(b) and still absorbs light at wavelengths above 1600 nm.

Tantalum monoboride behaves as a metallic ceramic with no bandgap with metallic behaviour [26]. Initial simulations were conducted using Quantum ATK software package based on the Slater-Koster model Hamiltonian [27]. Firstly, the atomic model of 6H-Silicon carbide was obtained from the Materials project website and atoms were added to the unit cell. Secondly, periodic lattices were chosen as boundary conditions of the simulation space, and more lattices were added along the c-axis (perpendicular to the hexagonal structure) until its length was about 30 angstroms. Thirdly, we repeated the procedure for tantalum monoboride until it reached a total length of more than 20 angstroms. The two materials were then bound together to create an interface. Two artificial electrodes were added to the simulation: although the real device is much larger than the atomic size simulated device, some initial prediction of the real device can be obtained. In Fig. S1, the molecule to the left is silicon carbide doped with nitrogen (nitrogen, silicon and carbon atoms are shown as dark blue, yellow, and grey spheres) and the molecule to the right is tantalum monoboride (light blue atoms

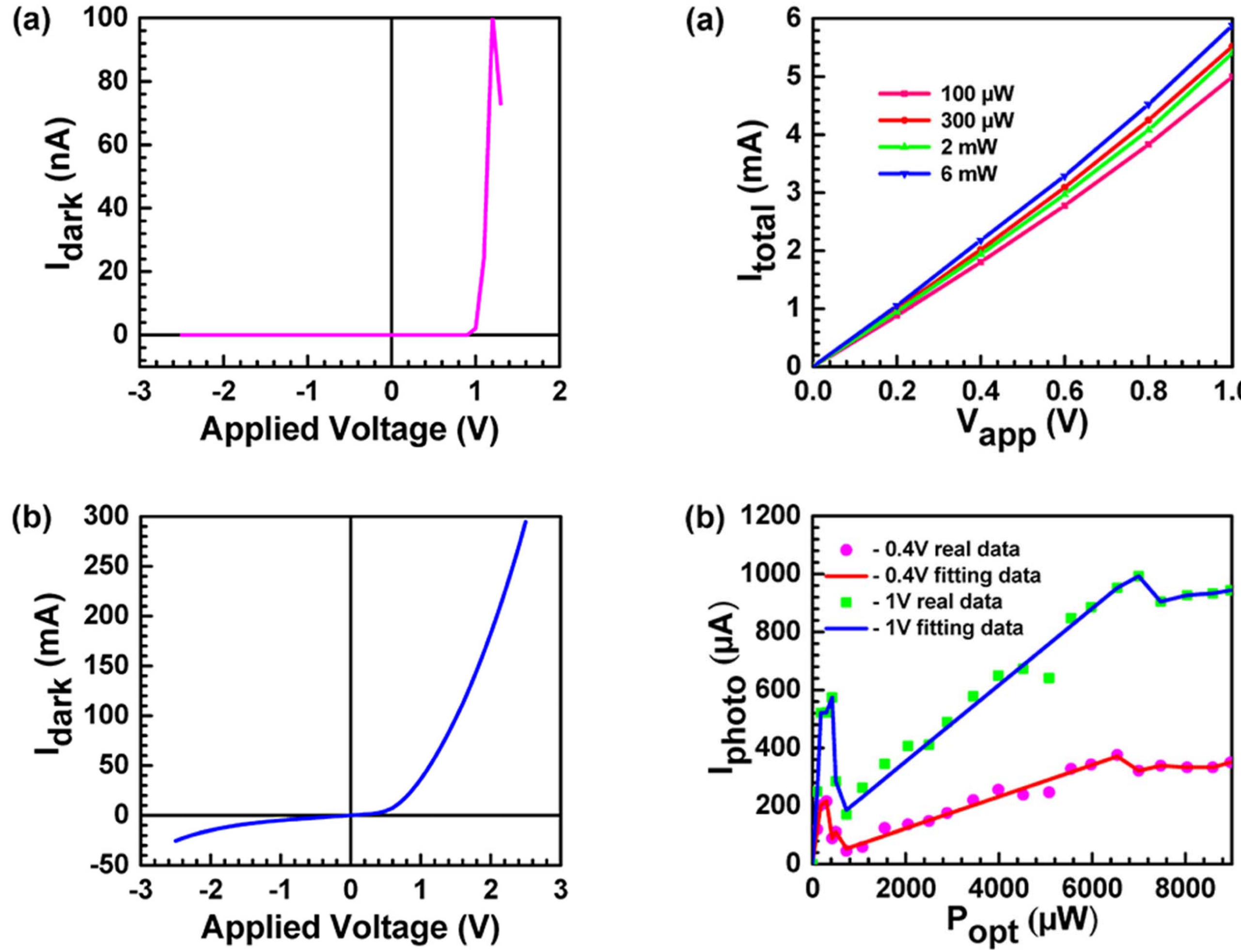

Fig. 4. (a) Simulated and (b) measured total current of the device.

Fig. 5. (a) Total current versus applied voltage for different optical power levels. (b) Absolute photocurrent versus incident optical power.

are boron and pink atoms are tantalum). The figure seems to indicate that, at the interface, covalent bonds are formed mostly between carbon and boron atoms, but sometimes also between carbon and tantalum atoms.

Fig. S2 shows the electron density inside the device. As shown in the Figure, electron density is significantly higher in silicon carbide region n-doped with nitrogen and significantly lower in the tantalum monoboride region, similarly to what happens in a p-n region in a semiconductor. In this sense, the *TaB* layer acts as a positively charged region, especially when the carbon and boron atoms form bonds.

Fig. 4(a) shows the theoretical dark current (I_{dark}) versus applied voltage (V_{app}) for a much smaller structure (50 angstroms length): while the current is significantly smaller than in the real device, some basic properties can be predicted through the simulation such as reverse bias current and built-in voltage. Based upon the Slater-Koster based Hamiltonian simulation, it is predicted that the built-in voltage will be around 1 V, and the reverse current will be low: the figure seems to indicate that the addition of a TaB layer onto the SiC substrate has created a p-n heterojunction. The measured *I-V* curve of the device (with the positive terminal on the TaB top electrode) shows that the device behaves as a kind of diode with a much gentler knee and a built-in voltage of around 1 V. After the diode conducts, the slope of the curve indicates that the forward-biased differential resistance is about 5.07 Ω. We have limited the maximum current to 300 mA to avoid damaging the device - in this current range, we have not observed any current saturation or dropping as predicted by the atomic level simulation. There is a reverse biased dark current which varies with the reverse voltage: the reverse current increases almost linearly with the voltage for applied voltages between 0 and -1 V (current of -5 mA at an applied voltage of -1 V) and then starts to increase exponentially (for example, the current is -14.8 mA at -2 V).

The photoresponse measurements were carried out for the constructed devices. As aforementioned, an S1FC405 laser source was used with a maximum power of 10 mW, while the beam exiting the fiber was collimated with a fiber collimator with output waist diameter of 1.10 mm. Since the output waist diameter is smaller than the dimensions of the device, it is reasonable to say that the device is fully illuminated by the optical beam. Fig. 5(a) shows the total current (I_{total}) as a function of the applied voltage (V_{app}) for different levels of

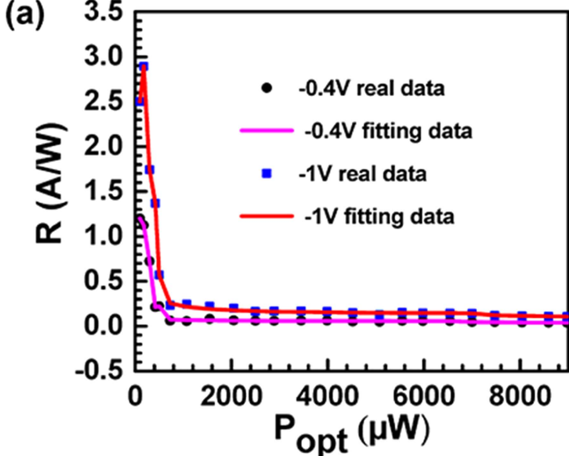

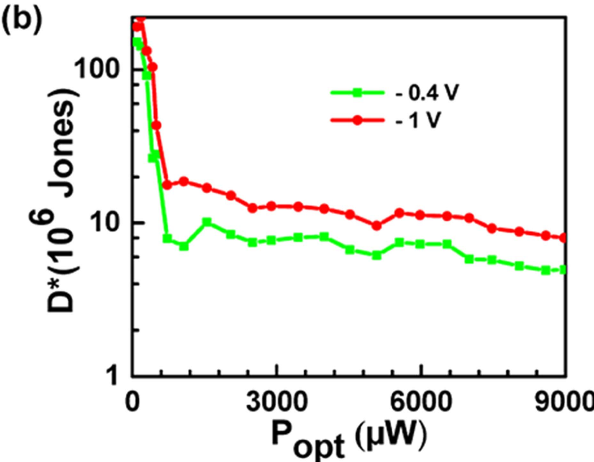

Fig. 6. (a) Responsivity and (b) detectivity as a function of the incident optical power at an applied voltage of -0.4 V (dotted curve) and -1 V (solid curve), respectively.

incident optical power: 100 μW, 300 μW, 2 mW and 6 mW. We have limited the applied voltage range between 0 and -1 V because when the applied voltage is above 0 V, the device is forward biased, while if the reverse bias voltage is below -1 V, the response becomes significantly more nonlinear. Fig. 5(b) shows the photocurrent (I_{photo}) as a function of the incident power (P_{opt}), where I_{photo} is defined as $I_{\text{photo}} = I_{\text{total}} - I_{\text{dark}}$: the blue curve represents a fitting curve for the measured data for an applied voltage of -1 V, while the red line represents a fitting curve for an applied voltage of -0.4 V. In the fitting curves, we have maintained the response for $P_{opt} < 730$ μW and $P_{opt} > 7$ mW, while we have fitted the curve between 730 μW and 7000 μW with a least square straight line using a Matlab function *polyfit*.

The first remark is that the photocurrent increases with the applied reverse bias, with significantly higher photocurrents at higher voltages: as observed in Fig. 6(a), the responsivity for powers between 730 μW and 7 mW (power densities of 78.77 W/m^2 and 755 W/m^2, respectively) increases from 0.06 to 0.15 A/W when the applied voltage is changed from -0.4 to -1 V (calculated by dividing the current by the incident power). For low powers (P_{opt}<730 μW), the responsivity is higher than in the linear region (for powers between 730 μW and 7 mW): similar response was observed by Wang et al. [28]. The explanation of the high responsivity at low powers can be attributed to the initial filling of defect and trap states that become filled at higher powers. In case of SiC, it has different types of defects such as vacancies and anti-sites [29], while TaB has also defects and trap states. In the linear region, after these states are filled, the photocurrent will be primarily produced by the generation of electron-hole pairs: based on Fig. 6(a), the linear responsivity is about 0.06 A/W at -0.4 V and 0.15 A/W at -1 V. If we consider that around 40% is not absorbed by the device (i.e., reflected) then the linear responsivity can potentially increase to 0.10 and 0.25 A/W at -0.4 V and -1 V, respectively (as a reference, a commercial broadband silicon carbide photodetector from Boston Electronics has a responsivity of 0.13 A/W). At powers above 7 mW, the device reaches saturation, and the current does not increase with the incident power since no more free carriers are available to generate more current. If responsivity (R) is defined as,

$$R = \eta \frac{q\lambda}{h_{\text{planck}} c_{\text{light}}} \tag{1}$$

where q is the elementary charge, η is the quantum efficiency, $\lambda = 405$ nm is the operating wavelength, h_{planck} is the Planck's constant and c_{light} is the speed of light in vacuum, then the quantum efficiency is 18% at -0.4 V and 46% at -1 V.

The detectivity (D^*) is an important parameter of the photodetector, which is calculated as [28],

$$D^* = R\sqrt{\frac{A_{\text{ilum}}}{2qI_{\text{dark}}}} \tag{2}$$

where A_{ilum} is the effective illuminated area. Fig. 6(b) shows D^* for two applied voltages: -0.4 V (dotted curve) and -1 V (solid curve): the detectivity is higher at -1 V albeit the fact that the dark current is higher at -1 V (5 mA against 1.8 mA at -0.4 V). D^* is higher at lower powers and does not change much for powers above 730 μW. The data points are represented by markers: rectangular markers at -0.4 V and circular markers at -1 V. The detectivity is high but not as high as other detectors: the detectivity could be further increased if the dark current is reduced from mA to nA. For example, the detectivity in the paper by Hu et al. [30] was in the order of 1.0×10^{10} Jones.

The spectral response of the fabricated detector is shown in Fig. 7. The responsivities at different wavelengths are normalized with respect to the responsivity at 405 nm and were measured by using different laser sources and the Keithley system. The green curve is for an applied voltage of -0.4 V, while the red curve is for a voltage of -1 V. The measurement seems to indicate a small drop in responsivity at around 500 nm, maybe due to the instability of the green laser used in the experiment. However, the responsivity is still reasonably high beyond 900 nm, indicating a potential operation beyond 900 nm (as indicated by Fig. 3(a)): measurements were limited to wavelengths below 1100 nm because of the light sources available in the lab.

Unfortunately, the 405 nm laser source cannot be modulated by a square wave because it may damage its internal power controller. To have at least some information about the time response of the fabricated photodetector, we have used a Q

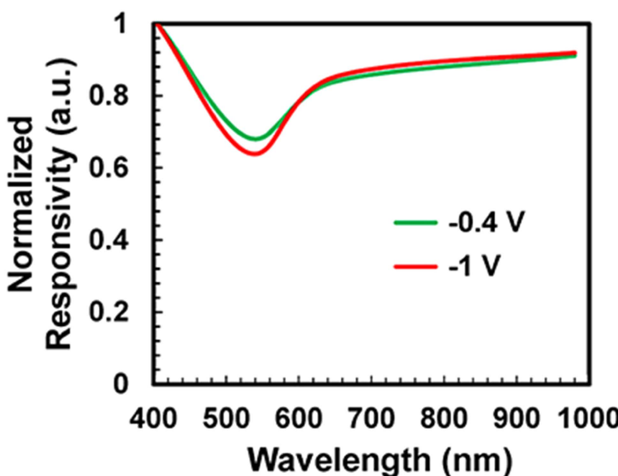

Fig. 7. Normalized responsivity as a function of the wavelength.

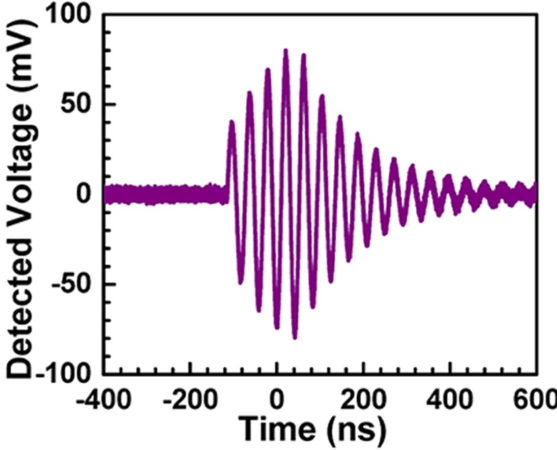

Fig. 8. Time response after the excitation by a 10 ns Q-switched pulse.

switched laser source with average power of 1 mW (an optical attenuator was used to reduce the average power) and repetition rate of 1 kHz. The pulse duration is 10 ns, with peak power (without attenuation) of 1500 W. The beam diameter is 2 mm, smaller than the fabricated device. Fig. 8 shows the response to the pulse: we have observed some oscillations of the pulse with frequency of 41.7 ns, while the pulse width of the envelope is about 260.7 ns. If we consider that the pulse width is given by [31]

$$\tau_{\text{total}} = \sqrt{\tau_{\text{initial}}^2 + \tau_{\text{response}}^2} \tag{3}$$

$$f_{\text{cutoff}} = \frac{1}{2\pi\tau_{\text{response}}} \tag{4}$$

with $\tau_{\text{initial}} = 10$ ns and $\tau_{\text{total}} = 260.7$ ns, then $\tau_{\text{response}} = 260.5$ ns and $f_{\text{cutoff}} = 610$ kHz.

Table I compares the performance of a few photodetectors with respect to the proposed device. The SiC nanobelt detectors [7] have very high responsivities but under lower power levels than the current work, leading to currents in the range of micro-amperes. They are also slower than the current work. A Ga_2O_3/GaN photodetector [9] had a responsivity of 0.5 A/W at a

TABLE I
COMPARISON OF PERFORMANCE OF DIFFERENT DETECTORS

Photo-detector	Test condition	Responsivity (mA/W)	Response time(s)	Dark Current (nA)	Ref.
B-doped 3C-SiC nanobelts	405 nm	6.37×10^8	50×10^{-3}	4.37×10^2	[7]
Ga_2O_3/ GaN	360 nm	5×10^2@2 V and 2.6×10^6 @ 16 V (very narrowband response)	0.1		[9]
Pt/Ni at NiO nanowire/ ZnO film	312 nm	17.0	2.9		[14]
PANI ZnO MW	380 nm at -3 V	37.0	50×10^{-6}	0.8×10^{-3}	[15]
Au@ ZnO	325 nm	0.45	12×10^{-3}	2×10^3	[16]
6H SiC/TaB	405 nm	2.9×10^3	260.5×10^{-9}	5×10^6 @-1 V	This work

voltage of 2 V, but drastically increased to 2580 A/W at 16 V after going through field-enhanced exciton ionization – however, the ionization resulted in a very narrow response over a 4 nm bandwidth and the device was slow. Other photodetectors [14], [15], [16] based upon ZnO have significantly lower responsivities and are slower than the current work, but they have significantly lower dark currents. In addition, the proposed device is easy to fabricate, and the p-n junction requires no doping in the p-side. Moreover, the device can handle direct currents above 300 mA.

IV. CONCLUSION

In this article, we propose a heterostructure by adding a 540 nm thick layer of TaB to a nitrogen n-doped silicon carbide substrate for high-performance near UV photodetection. The carbon atoms of silicon boride form bonds with the boron and tantalum atoms in the TaB layer, with a reasonably smooth interface between TaB and SiC. The heterostructure works as a rectifier device that could handle electrical currents above 300 mA and built-in voltage of around 1 V. The dark current at −0.4 and −1 V are about 1.8 and 5 mA, respectively; while the responsivity is about 3.0 A/W at low powers, dropping to 0.2 A/W at higher powers. The fabricated device seems to be able to work at frequencies as high as 610 kHz. The device provides a new path for high-performance photodetection of near-UV light in potential sensing applications and harsh environments.

REFERENCES

[1] Y. Yamazaki et al., “Carrier dynamics of silicon vacancies of SiC under simultaneous optically and electrically excitations,” *Appl. Phys. Lett.*, vol. 118, no. 2, 2021, Art. no. 021106.

[2] T. Kimoto and J. A. Cooper, *Fundamentals of Silicon Carbide Technology: Growth, Characterization, Devices and Applications*. Singapore: Wiley, 2014.

[3] B. J. Baliga, *Gallium Nitride and Silicon Carbide Power Devices*. Singapore: World Sci., 2016.

[4] L. Tong et al., "Stable mid-infrared polarization imaging based on quasi- 2D tellurium at room temperature," *Nature Comm.*, vol. 11, 2020, Art. no. 2308.

[5] L. Tong et al., "2D materials-based homogeneous transistor-memory architecture for neuromorphic hardware," *Science*, vol. 373, pp. 11353–11358, 2021.

[6] Y. Shen et al., "Near ultraviolet enhanced 4H-SiC schottky diode," *Appl. Phys. Lett.*, vol. 115, no. 26, 2019, Art. no. 261101.

[7] T. Yang et al., "High performance SiC Nanobelt photodetectors with long term stability against 300 °C up to 180 days," *Adv. Func. Mater.*, vol. 29, 2019, Art. no. 1806250.

[8] T. Oshima, T. Okuno, N. Arai, Y. Kobayashi, and S. Fujita, "β-Al2xGa2-2xO3 thin film growth by molecular beam epitaxy," *Jpn. J. Appl. Phys.*, vol. 48, no. 7R, 2009, Art. no. 070202.

[9] R. Tang et al., "Ga2O3/GaN heterostructural ultraviolet photodetectors with exciton-dominated ultranarrow response," *ACS Appl. Electron. Mater.*, vol. 4, no. 1, pp. 188–196, 2022.

[10] X. Tang et al., "Quasi-epitaxial growth of β-Ga2O3-coated wide band gap semiconductor tape for flexible UV photodetectors," *ACS Appl. Mater. Interfaces*, vol. 14, no. 1, pp. 1304–1314, 2022.

[11] P. Reddy et al., "High gain, large area, and solar blind avalanche photodiodes based on Al-rich AlGaN grown on AlN substrates," *Appl. Phys. Lett.*, vol. 116, no. 8, 2020, Art. no. 081101.

[12] A. K. Das, V. K. Sahu, R. S. Ajimsha, and P. Misra, "A model for surface space charge mediated ultraviolet photoresponse in MgZnO thin films and its experimental verification," *ACS Appl. Electron. Mater.*, vol. 2, no. 3, pp. 651–658, 2020.

[13] W. Ouyang et al., "Self-powered UV photodetectors based on ZnO nanomaterials," *Appl. Phys. Rev.*, vol. 8, no. 3, 2021, Art. no. 031315.

[14] Y. Luo et al., " Self-powered NiO@ZnO-nanowire heterojunction ultraviolet photodetector," *Opt. Mater. Exp.*, vol. 9, pp. 2775–2784, 2019.

[15] Y. Chen, L. Su, M. Jiang, and X. Fang, "Switch type PANI/ZnO core-shell microwire heterojunction for UV phtodetection," *J. Mater. Sci. Technol*, vol. 105, pp. 250–265, 2022.

[16] J. Meng, Q. Li, J. Huang, C. Pan, and Z. Li, "Self-powered photodetector for ultralow power density UV sensing," *Nano Today*, vol. 43, 2022, Art. no. 101399.

[17] H. Chen, K. Liu, L. Hu, A. A. Al-Ghamdi, and X. Fang, "New concept ultraviolet photodetectors," *Mater. Today*, vol. 18, pp. 493–502, 2015.

[18] L.-Z. Qiu et al., "Ultrathin polymer nanofibrils for solar-blind deep ultraviolet light photodetectors application," *Nano Lett.*, vol. 20, no. 1, pp. 644–651, 2020.

[19] G. V. Samsonov, P. Hagenmuller, and V. I. Matkovich, *Boron and Refractory Borides*. Berlin, Germany: Springer, 2012.

[20] W. G. Fahrenholtz, E. J. Wuchina, W. E. Lee, and Y. Zhou, *Ultra-high Temperature Ceramics*. Hoboken, NJ, USA: Wiley, 2014.

[21] S. Okada, K. Kudou, I. Higashi, and T. Lundström, "Single crystals of TaB, Ta5B6, Ta3B4 and TAB2, as obtained from high-temperature metal solutions, and their properties," *J. Cryst. Growth*, vol. 128, no. 1, pp. 1120–1124, 1993.

[22] S. Motojima, K. Kito, and K. Sugiyama, "Low-temperature deposition of TaB and TaB2 by chemical vapor deposition," *J. Nucl. Mater.*, vol. 105, no. 2, pp. 262–268, 1982.

[23] S. Wang et al., "4H-SiC: A new nonlinear material for midinfrared lasers," *Laser Photon. Rev*, vol. 7, no. 5, pp. 831–838, 2013.

[24] A. Haque et al., "Broadband and thermally stable tungsten boride absorber," *J. Opt. Soc. Amer. B*, vol. 36, no. 10, pp. 2744–2749, 2019.

[25] D. Ren et al., "Uncooled photodetector at short-wavelength infrared using InAs nanowire photoabsorbers on InP with p–n heterojunctions," *Nano Lett.*, vol. 18, no. 12, pp. 7901–7908, 2018.

[26] Accessed: Jan. 8, 2023. [Online]. Available: http://www.materialsproject.org/materials/mp-1097

[27] D. A. Papaconstantopoulos and M. J. Mehl, "The Slater–Koster tight-binding method: A computationally efficient and accurate approach," *J. Phys. Condens. Matter*, vol. 15, no. 10, Art. no. R413, 2003.

[28] F. Wang et al., "High-responsivity vis–NIR photodetector based on a Ag2S/CsPbBr3 heterojunction," *ACS Appl. Electron. Mater.*, vol. 4, no. 8, pp. 3922–3929, 2022.

[29] M. E. Bathen et al., "Characterization methods for defects and devices in silicon carbide," *J. Appl. Phys.*, vol. 131, no. 14, 2022, Art. no. 140903.

[30] H. Hu et al., "Improved photoelectric performance with self-powered characteristics through TiO2 surface passivation in an α-Ga2O3 nanorod array deep ultraviolet photodetector," *ACS Appl. Electron. Mater.*, vol. 4, no. 8, pp. 3801–3806, 2022.

[31] H. Walman, "Transient response and the central limit theorem of probability," *Proc. Symposia Appl. Math.*, vol. 2, 1950, Art. no. 91.